An Improved Equivalent Circuit Model of a Single-Sided Linear Induction Motor

Wei Xu, *Member, IEEE*, Jianguo Zhu, *Senior Member, IEEE*, Yongchang Zhang, Yaohua Li, Yi Wang, and Youguang Guo, *Senior Member, IEEE*

***Abstract*—The derivation of the equivalent circuit for a single-sided linear induction motor (SLIM) is not straightforward, particularly if it includes longitudinal end effects from the cut-open primary magnetic path, transversal edge effects from the differing widths between the primary lamination and secondary sheet, and half filled primary slots. This paper proposes an improved series equivalent circuit for this machine. The longitudinal end effects are estimated using three different impedances representing the normal, forwards and backwards flux density waves in the air-gap, whose two boundary conditions are deduced by introducing the conception of magnetic barrier surface. The transversal edge effects are accounted by correction coefficient $\overline{K_t}$ and an air-gap flux density correction coefficient $\overline{K_b}$. Using the series circuit, the performance of the SLIM was assessed in a similar manner to a rotating induction machine. A 4 kW SLIM prototype was tested which validated the simulation technique.**

***Index Terms*—Equivalent circuit, linear metro, longitudinal end effects, single-sided linear induction motor (SLIM), transversal edge effects.**

NOMENCLATURE

σ	Conductivity of secondary sheet
ω	Angular frequency of power supply
τ_e	Half-wave length of end-effect wave
α_1	Length of entry-end-effect wave penetration coefficient
α_2	Length of exit-end-effect wave penetration coefficient
ε_0	Primary phase inducted electromotive force
τ	Pole pitch
b_y	y-axis magnetic flux density
g	Equivalent air-gap length
g_m	Mechanical air gap length
l_w	Width of primary lamination
m	Phase number
q	Number of coil sides per phase per pole
s	Per-unit slip
v_s	Motor synchronous speed
w_1	Number of turns per phase for primary winding
B_0	Amplitude for magnetic flux density of normal wave
B_1	Amplitude for magnetic flux density of entry-end-effect wave
B_2	Amplitude for magnetic flux density of exit-end-effect wave
E_0	Primary induced electromotive force per phase by normal electric field intensity
E_1	Primary induced electromotive force per phase by entry-end electric field intensity
E_2	Primary induced electromotive force per phase by exit-end electric field intensity
F_{e0}	Fundamental-wave thrust
F_Ω	Fundamental-wave mechanical thrust
F_{e1}	Entrance-wave thrust
F_{e2}	Exit-wave thrust
G	Goodness factor
J_1	Equivalent primary current sheet
L_p	Primary length
K_p	Half-filled slot correct coefficient
K_{w1}	Winding coefficient of primary winding
P	Number of factual primary pole pairs
P_e	Number of equivalent primary pole pairs
P_{m1}	Electromagnetic power by entrance flux density wave
P_{m2}	Electromagnetic power by exit-end flux density wave
X_m	Phase magnetizing reactance
Z_m	Primary Phase magnetizing impedance
$\mathbf{Z}_L$	Total equivalent longitudinal end-effect impedance
$\mathbf{Z}_{Lc}$	Correct longitudinal end-effect impedance
$\mathbf{Z}_{mc}$	Correct fundamental impedance
$\mathbf{Z}_t$	Total circuit impedance

W. Xu, J.G. Zhu, Y.C. Zhang, Y. Wang, Y.G. Guo are with the School of Electrical, Mechanical and Mechatronic Systems, University of Technology Sydney, Australia (e-mail: wxu@eng.uts.edu.au; joe@eng.uts.edu.au).

Y.H. Li is with the Institute of Electrical Engineering, Chinese Academy of Sciences, Beijing, China (e-mail: yhli@mail.iee.ac.cn).

I. INTRODUCTION

SINGLE-sided linear induction motors (SLIMs) are derived from rotating induction motors (RIMs). The SLIM's primary side can be simply regarded as a rotary induction motor (RIM) stator which is cut-open and rolled flat. The secondary side is similar to the RIM rotor which often consists of a sheet conductor, such as copper or aluminum, with a solid back iron acting as the return path of the magnetic flux. The thrust corresponding to the RIM torque can be produced by the reaction between the air gap flux density and the eddy current in the secondary sheet [1, 2].

SLIMs have been utilized in a number of applications especially in the electromechanical energy conversion units, such as horizontal conveyance system [3], baggage handling system [4], elevator vertical drive system [5], liquid metal pumps [6, 7], aircraft launch or accelerator system [8], low speed low-head hydro (water-wheel) generation where the copper or aluminum secondary plate is on the large-diameter wheel, and so

on. In recent years, a train driven by SLIM as illustrated in Fig.1, usually called as linear metro, has been paid more attention by academia and industry than before. It can be seen that the SLIM primary is hanged below the redirector, which is supplied by the inverter on the vehicle. The secondary is flattened on the railway track, which consists of a 5 mm thick copper/aluminum conductance fleet and a 20 mm thick back iron. When the primary three-phase windings are input with AC current, they can build up air gap flux linkage and induce eddy current in the secondary sheet. This eddy current will react with aforementioned air gap flux linkage so as to produce horizontal electromagnetic thrust that can drive the vehicle forward directly without friction between wheel and track.

By now, there are more than 20 commercial linear metro lines of about 400 kilometers in the world, such as the Kennedy air line in America, the linear metro in Japan, the Vancouver light train in Canada, the Guangzhou subway line 4 and the Beijing airport rapid transport line in China, and so on. The SLIM drive system has the following merits compared with the RIM drive [9-16]. Firstly, it can achieve direct propulsive thrust, which is not dependent on the friction between wheel and rail. Secondly, it has smaller turning radius, smaller cross-sectional area for requirement of a tunnel, larger acceleration, and stronger climbing ability. By investigations from some Japanese experts, the typical SLIM drive system has 40-60 m turning radius, 22 m^2 cross-sectional tunnel area, 1.2 m/s^2 acceleration, and 6-8% gradient ability compared with the 80-120 m turning radius, 41 m^2 cross-sectional tunnel area, 0.8 m/s^2 acceleration, and 3-4% gradient ability in a typical RIM drive system. Thirdly, it has lower noise and less maintenance. Hence, the SLIM drive system is very suitable to the transportation in large cities.

The SLIM's special structure means that its performance is a little different from that of an RIM [17, 18]. As we know, in the RIM, an accurate equivalent circuit model can be derived easily based on the symmetrical geometry per pole. Unfortunately, it is not as straightforward to gain the equivalent circuit for an SLIM mainly for the following three causes.

(1) As the SLIM primary moves, a new flux is continuously developed at the primary entrance side, while the air gap flux disappears quickly at the exit side. By the influence of the sudden generation and disappearance of the air gap penetrating flux density, an amount of eddy current in anti-direction to the primary current will occur in the secondary sheet, which correspondingly affects the air gap flux profile along the longitudinal direction (*x*-axis) [9, 15]. This phenomenon is called "longitudinal end effects", which could increase the copper loss, and decrease the mutual inductance as the velocity goes up. In the end, the effective electromagnetic thrust will be reduced because of its attenuated air gap average flux linkage [16].

(2) The different width between primary lamination and secondary sheet can result in non-uniform flux density, which may increase the secondary equivalent resistance. The phenomenon is named as "transversal edge effects".

(3) For the cut-open primary magnetic circuit, there exist half-filled slots in the primary ends. Hence, three-phase magnetic circuits are not symmetrical with each other. Three-phase currents are not symmetrical even when excited by three-phase balanced voltages. The half-filled slots will affect the air gap flux density distribution so as to result in some alteration in mutual inductance, leakage inductance, and secondary equivalent resistance.

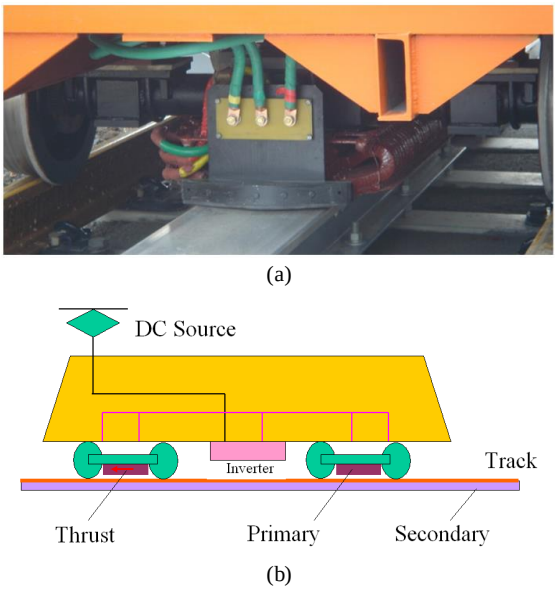

Fig. 1. Simple vehicle system diagrams propelled by the SLIM. (a) Photo of an SLIM driven vehicle. (b) Diagram of the drive system.

Thanks to many researchers' work in the past several decades, plenty of papers have been available on the analysis of the SLIM equivalent circuit. Ref. [19] developed a simple model for SLIM high performance control, which requires only several structure or equivalent circuit parameters, i.e. number of poles, pole pitch, primary resistance & leakage inductance, magnetizing inductance, and secondary resistance & leakage inductance. However, the model is not suitable to electromagnetic performance analysis for its coarse approximation of longitudinal end effect and without considering equivalent airgap variation. Ref. [20] proposed a simple equation for the end effect factor to modify the airgap EMF, which is sufficiently accurate to be used for design studies of SLIMs. However, the end effect factor without considering the half-filled slot effect is closely dependent on the designer experience, which could bring some calculation error especially in high speed region. One comprehensive model using coupled FEM and control algorithm taking into account the movement was proposed in [21]. In finite element region instead of the voltage equation, the primary flux linkage affected by longitudinal end effect can be calculated directly. This model can be adapted to study SLIM performance with reasonable accuracy, but it is not efficient to design SLIM for its great time consumption, especially in optimal design procedure. Ref. [22] presented a single phase T-model equivalent circuit to study the SLIM steady performance. Based on the one dimensional numerical analysis, two coefficients are derived to describe the

influence of the longitudinal end effect on the mutual inductance and secondary equivalent resistance. This model can be adopted in a wide speed region and with different air gap lengths. Unfortunately, the coefficients dependent of experimentation cannot be gained accurately in most cases, which might bring great error to the performance analysis. Refs. [1] and [23] presented one useful function according to the secondary eddy current average value and energy conversion balance theorem. The function is affected by the SLIM speed, secondary resistance, secondary inductance, and some structural parameters, such as the primary length. However, the function derivation process supposing air gap flux in decaying exponential form is not accurate, which brings an increasing error in some key parameters like torque as its velocity goes up. One model by using space harmonic method can theoretically simulate SLIM performance with comparatively high accuracy [2]. However, it requires substantially more computing time to gain some useful information, and the calculation accuracy depends closely on some initially given parameters. If some key values are not initialized rationally, the final solution cannot be obtained due to non-convergence.

This paper uses the air-gap flux density equation to develop an improved series equivalent circuit which considers the influences of the entry and exit end-wave flux waves in the air-gap, as well as transversal edge effects, half filled slots and air-gap leakage flux. The equivalent circuit based on one dimensional model is comparatively simple and reasonably accurate to analyze the performance of SLIM applied in linear metro.

This paper is organized as follows. The SLIM physical model is described in Section II. The equivalent series circuit is developed in Section III. In Section IV, the results of simulation and experimentation are discussed in detail. Finally, the paper is summarized in Section V.

The notation used in the paper is fairly standard. One plural is expressed in the form of $\overline{A} = x + jy$,where x is the real part, y the imaginary part, and j the notation of imaginary part. One vector is expressed in the form of $\vec{A} = \vec{i}x + \vec{j}y + \vec{k}z$, where $\vec{i}$, $\vec{j}$, $\vec{k}$ are the notations of x-, y-, z-, axis directions.

II. PHYSICAL MODEL

To simplify the analysis, some assumptions are used [22-30]:

(a) The stator iron has infinite permeability. The material of stator iron is silicon-steel sheet with 0.5 or 0.2mm thickness, whose permeability is about 2 000 times that of air gap or larger, so in most cases, the permeability of stator iron can be considered infinite.

(b) Skin effect is neglected in the secondary. The primary rated frequency of SLIM especially applied in transportation is about 50 Hz, and the typical slip is near 0.2. Hence, the secondary frequency (slip frequency) is close to 10 Hz. Skin effect of the secondary in such low frequency is not obvious.

(c) Winding space harmonics are negligible. Winding space harmonics is related with the primary winding distribution, which can be reduced by optimal winding arrangement during the electromagnetic design procedure. Furthermore, it can be further reduced by relative harmonics elimination control schemes.

(d)The primary and secondary currents flow in infinitesimally thin sheets. By field theories of electrical machine, the winding current or eddy current can be usually represented by current sheets without thickness. The primary or secondary eddy current is actually discrete quantity, while the current sheet is continuous. If they can produce the same magnetomotive force, they will be equivalent to each other.

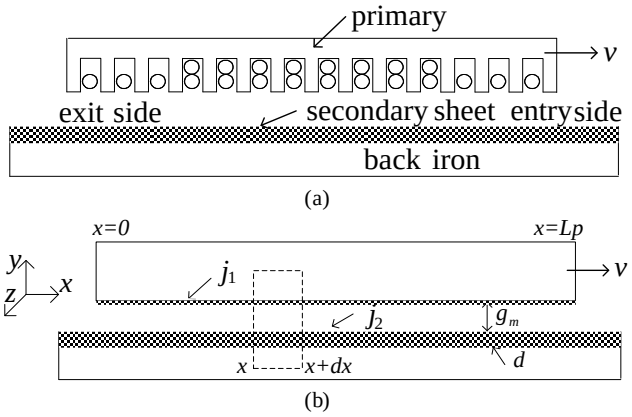

Fig. 2. The structure and one-dimensional analytic model of SLIM. (a). Structure. (b).Model.

The structure and one-dimensional representation of the SLIM are shown in Fig. 2. The model described in [26] derives several relevant coefficients for the secondary sheet current and air-gap flux density. The analysis from [27] can be used to analyze the system. From Ampere's Law (with reference to the geometry in Fig. 2):

$$\frac{g}{\mu_0}\frac{\partial b_y}{\partial x} = j_1 + j_2 \tag{1}$$

where j_1 is the primary current, j_2 the secondary current, by y-axis airgap magnetic fluxdensity, g the airgap equivalent length, and μ_0 the air permeability. We can implement a one-dimensional Curl function for the secondary plate - the air-gap electric field has to be referred to the secondary [26, 27]:

$$\frac{\partial e_z'}{\partial x} = \frac{\partial b_y}{\partial t} + \frac{\partial b_y}{\partial x}\frac{\partial x}{\partial t} = \frac{\partial b_y}{\partial t} + v\frac{\partial b_y}{\partial x} \tag{2}$$

where the second term on the right hand side is the speed term. Referring the secondary current sheet to the primary, we can obtain an expression for the air-gap flux density in terms of the (measureable) primary current. The secondary normally consists of a copper or aluminum conducting sheet and we will assume that the current is resistance-limited. Then e_z' can be expressed by the secondary current j_2 and surface conductivity σ:

$$e_z' = \frac{j_2}{\sigma} \tag{3}$$

where $\sigma = d/\rho$ (in ohm) , d is the thickness of secondary

conductance sheet, and ρ is the volume resistivity (in ohm-m). We can combine the aforementioned equations so that

$$g\frac{\partial^2 b_y}{\partial x^2}-\sigma\mu_0 v\frac{\partial b_y}{\partial x}-\sigma\mu_0\frac{\partial b_y}{\partial t}=\mu_0\frac{\partial j_1}{\partial x} \tag{4}$$

If we assume that the primary current j_1 in form of cosine function can be expressed by,

$$j_1=j_1(x,t)=\mathrm{Re}\left\{\bar{J}_1 e^{j(\omega t-\pi x/\tau)}\right\} \tag{5}$$

then we can obtain an expression for the air-gap flux density by combining (4) and (5):

$$g\frac{\partial^2 b_y}{\partial x^2}-\sigma\mu_0 v\frac{\partial b_y}{\partial x}-j\sigma\mu_0\omega b_y=\mathrm{Re}\left\{-j\mu_0\frac{\pi}{\tau}J_1 e^{j(\omega t-\pi x/\tau)}\right\} \tag{6}$$

where $j\sigma\mu_0\omega b_y$ comes from the differential operation of b_y to time.

The solution of b_y based on (4) is

$$b_y=b_y(x,t)=\mathrm{Re}\left\{\left(\bar{B}_0 e^{-j\frac{\pi x}{\tau}}+\bar{B}_1 e^{-\frac{x}{\alpha_1}}e^{-j\frac{\pi x}{\tau_e}}+\bar{B}_2 e^{\frac{x}{\alpha_2}}e^{j\frac{\pi x}{\tau_e}}\right)e^{j\omega t}\right\} \tag{7}$$

The flux density b_y includes three parts: b_0, b_1 and b_2 [22, 28-32]. b_0 is the normal traveling wave which moves forward in a similar manner to the fundamental flux density wave in a rotating induction machine (RIM). The fundamental wave b_0 in the same amplitude transmits with synchronous speed, $2f\tau$. b_1 and b_2, the entrance and exit end-effect waves, are determined from two boundary conditions, which are discussed in appendix I. Generally speaking, b_1 is a gradually attenuating wave traveling along the x-axis. Its attenuation constant is $1/\alpha_1$ and the end-effect half-wave length is τ_e. b_2 travels along the x-axis in the negative direction with an attenuation constant of $1/\alpha_2$. The transmitting speeds of forward and backward waves, b_1 and b_2, are $2f\tau_e$ [27, 31].

We can derive the air-gap fundamental flux density coefficient $\bar{B}_0$ based on the homogeneous equation of (4), which can be described as

$$\bar{B}_0=\frac{j\tau\mu_0\bar{J}_1}{g\pi(1+jsG)} \tag{8}$$

where G is goodness factor deduced as in appendix II, $G=\dfrac{\sigma\mu_0\omega\tau^2}{g\pi^2}$, and the slip $s=(v_s-v)/v_s$. we need to define the synchronous velocity $v_s=\omega\tau/\pi$ with pole pitch τ. The coefficients of entrance and exit waves, $\bar{B}_1$ and $\bar{B}_2$, can be gained by two boundary conditions in primary area based on introducing magnetic barrier surface, which is discussed in appendix I. Briefly, the expressions of $\bar{B}_1$ and $\bar{B}_2$ can be summarized here.

$$\bar{B}_1=j\frac{\tau}{\pi}\left(\frac{1}{\alpha_1}+j\frac{\pi}{\tau_e}\right)\bar{B}_0 \tag{9}$$

where $\alpha_1=\dfrac{2g}{Xg-\sigma\mu_0 v}$, and $\tau_e=\dfrac{2\pi}{Y}$ .We can define $X+jY=\sqrt{\left(\dfrac{\sigma\mu_0 v}{g}\right)^2+4j\dfrac{\sigma\mu_0\omega}{g}}$.

In a similar fashion

$$\bar{B}_2=-j\frac{\tau}{\pi}e^{-\left(\frac{1}{\alpha_2}+j\frac{\pi}{\tau_e}\right)L_p}\left(\frac{1}{\alpha_2}+j\frac{\pi}{\tau_e}\right)\bar{B}_0 \tag{10}$$

where $\alpha_2=\dfrac{2g}{Xg+\sigma\mu_0 v}$.

We now have a complete definition of the air-gap flux-density wave in terms of the stator surface current density. Most parameter definitions from (1) to (10) are given in Nomenclature. The curves for α_1, α_2 and τ_e are shown in Fig. 3, which are similar to those of [25]. It is assumed that the SLIM operates from zero to 100 m/s, and the secondary copper sheet equivalent surface resistivity (=ρ/d) is 5.63×10^{-5} ohm where the sheet thickness d is 3 mm. From Fig. 3 (a), the length of the entry wave penetration coefficient α_1 increases with motor velocity v. It is close to 0.4 m when the equivalent air-gap length g is 10 mm and v is 10 m/s. However, the length of the exit wave penetration coefficient α_2 in Fig. 3 (b) decreases with increasing motor velocity, and it is almost 2 mm when g is 10mm and v is 10 m/s. From Fig. 3 (c), the half-wave length τ_e of the end-effect wave increases with velocity, is close to 0.1 m when g is 10 mm and v is 10 m/s. Hence, the entry end effect wave, b_1, can transmit along the primary length area which is almost equal in amplitude and opposite in phase to the normal wave, b_0. The former wave can reduce the average air gap flux density so as to bring negative effect to the performance. The exit end effect wave, b_2, can only transmit in a very limited distance close to the exit end, which could bring comparatively small influence to SLIM operation.

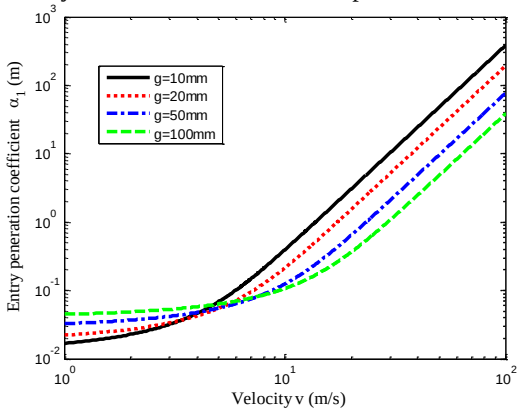

(a)

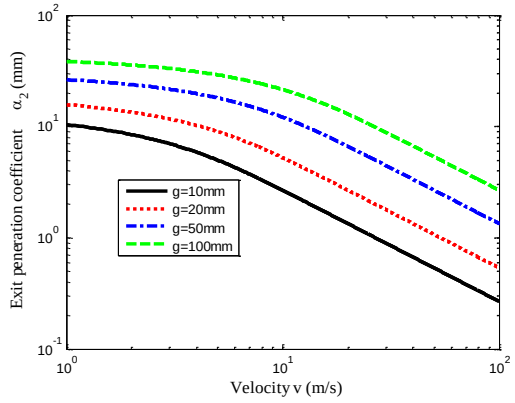

(b)

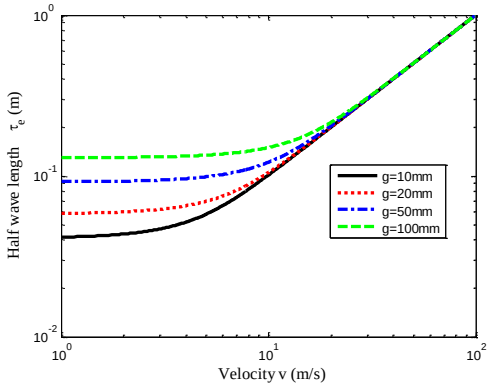

(c)

Fig. 3. Penetration coefficients and half-wave length versus motor velocity.
(a) Entry penetration coefficient α_1. (b) Exit penetration coefficient α_2. (c) Half-wave length τ_e.

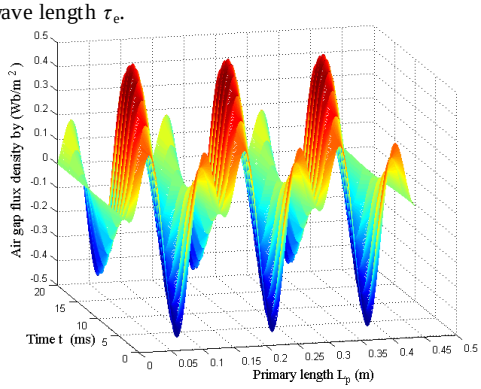

Fig. 4. Air gap flux density distribution in the primary length (6-pole wave progression illustrated).

Fig. 4 shows a SLIM air-gap flux density distribution for the machine studied here over the primary length area in different time. The final flux wave is not sinusoidal because of the influence of the entry and exit flux waves.

The electric field intensity in the air-gap is denoted by (2). However, this now needs to be referred to primary where the coordination is relatively still to the primary. Hence, the speed term in the right side of (2) can be ignored, and then we can get

$$e_z(x,t)=\int\frac{\partial b_y}{\partial t}\partial x=\mathrm{Re}\left\{\begin{array}{l}\bar{E}_0e^{j\left(\omega t-\frac{\pi x}{\tau}\right)}+\bar{E}_1e^{-\frac{x}{\alpha_1}}e^{j\left(\omega t-\frac{\pi x}{\tau_e}\right)}\\+\bar{E}_2e^{\frac{x}{\alpha_2}}e^{j\left(\omega t+\frac{\pi x}{\tau_e}\right)}\end{array}\right\} \tag{11}$$

With the knowledge of the air-gap flux density distribution, the electric field intensity produces three terms: $\boldsymbol{E}_0$, $\boldsymbol{E}_1$ and $\boldsymbol{E}_2$ which are deduced in appendix I. These individually produce an induced electromotive force in the machine windings so that $\bar{E}_0=-\omega\frac{\tau}{\pi}\bar{B}_0$, $\bar{E}_1=-\frac{j\omega\bar{B}_1\alpha_1\tau_e}{(\tau_e+j\pi\alpha_1)}$, and $\bar{E}_2=\frac{j\omega\bar{B}_2\alpha_2\tau_e}{\tau_e+j\pi\alpha_2}$.

III. Equivalent Circuit

The equivalent circuit is essential for analyzing the motor and predicting its performance. It is particularly necessary for the initial SLIM electromagnetic design procedure. Here the induced electromotive force is used to compute the fundamental-wave impedance. The complex power and electric-magnetic thrust methods are adapted to derive the entrance- and exit-wave impedances, which are utilized to calculate the SLIM thrust, power factor, efficiency and other performance parameters.

A. Fundamental-wave Impedance

The fundamental elements such as excitation current, electric field intensity and flux density are assumed to be sinusoidal shown below. From [27, 32], the entrance and exit-wave elements, such as $b_1(x,t)$, $b_2(x,t)$, $e_1(x,t)$, $e_2(x,t)$, have similar forms. In order to simplify the derivation procedure, we can use the following equations to represent the current, air-gap flux density and electric fields:

$$j_1(x,t)=\mathrm{Re}\left\{\bar{J}_1e^{j\left(\omega t-\frac{\pi x}{\tau}\right)}\right\} \tag{12}$$

$$b_0(x,t)=\mathrm{Re}\left\{\bar{B}_0e^{j\left(\omega t-\frac{\pi x}{\tau}\right)}\right\} \tag{13}$$

$$e_0(x,t)=\mathrm{Re}\left\{\bar{E}_0e^{j\left(\omega t-\frac{\pi x}{\tau}\right)}\right\} \tag{14}$$

The magnetic motive force $F(x, t)$ is of a similar form:

$$F(x,t)=\mathrm{Re}\left\{j\frac{g\tau}{\pi}J_1e^{j\left(\omega t-\frac{\pi x}{\tau}\right)}\right\} \tag{15}$$

The relationship between primary current sheet J_1 and phase current I is

$$\bar{J}_1=J_1=\frac{\sqrt{2}mw_1K_{w1}}{\tau P}I \tag{16}$$

where P is the factual number of pole pairs. The equivalent continuous current sheet can produce the same sinusoidal

magnetomotive force as that of the primary discrete concentrative winding current. If we assume that the reference current is a real value, the induced phase electromotive force is

$$\bar{\varepsilon}_0 = j\sqrt{2}w_1 K_{w1} l_w \bar{E}_0 \tag{17}$$

The fundamental-wave impedance can be calculated:

$$\bar{Z}_m = \frac{\bar{\varepsilon}_0}{I} = \frac{jX_m}{(1+jsG)} \tag{18}$$

where X_m is

$$X_m = \frac{4mf(w_1 K_{w_1})^2 l_w \tau \mu_0}{P\pi g} \tag{19}$$

The fundamental-wave thrust F_{e0} is denoted by

$$F_{e0} = \frac{l_w}{2}\mathrm{Re}\int_0^{L_p} \bar{B}_0 e^{-j\frac{\pi x}{\tau}} \left\{ \bar{J}_1 e^{-j\frac{\pi x}{\tau}} \right\}^* .dx = \frac{mI^2 \mathrm{Re}\{\bar{Z}_m\}}{v_s} \tag{20}$$

where the integral length along the primary length $L_p = 2P\tau$. The mechanical power can be obtained from (20) by multiplying the speed v. But $v = (1 - s)v_s$ so that the mechanical power becomes

$$P_{m0} = mI^2 \mathrm{Re}\{(1-s)\bar{Z}_m\} \tag{21}$$

We can investigate $\mathbf{Z}_m$ in (18). If we follow through some rearrangement of (18), we can obtain

$$\bar{Z}_m = \frac{jX_m}{(1+jsG)} = \frac{jX_m\left(r_2/s\right)}{\left(r_2/s + jX_m\right)} = \frac{jX_m}{\left(1+sjX_m/r_2\right)}$$

From this the rotor resistance (referred to the stator) is

$$r_2 = \frac{2m\left(w_1 K_{w1}\right)^2 l_w}{\sigma\tau P}$$

This derivation illustrates that the theory is similar to the standard equivalent circuit analysis for rotating machines. Because the secondary is a simple copper plate, the secondary inductance is assumed negligible and the current is resistance limited.

B. Entrance-wave Impedance

The electromagnetic power P_{m1} for the y-axis entrance flux wave is the power flowing into the rotor through this wave:

$$P_{m1} = \frac{l_w}{2}\mathrm{Re}\int_0^{L_p} -\bar{E}_1 e^{-\frac{x}{\alpha_1}} e^{-j\frac{\pi x}{\tau_e}} .\left\{ \bar{J}_1 e^{-j\frac{\pi x}{\tau}} \right\}^* .dx \tag{22}$$

so that

$$P_{m1} = \mathrm{Re}\left\{ mI^2 \left(\overline{K}_1 \bar{Z}_m\right)\right\} \tag{23}$$

where

$$\overline{K}_1 = -\frac{\alpha_1}{2P}\left(\frac{\tau_e}{\tau\tau_e + j\alpha_1\pi\left(\tau - \tau_e\right)}\right). \tag{24}$$

However, the entrance-wave thrust F_{e1} can be used to derive how much of P_{m1} is converted into mechanical power. This is similar to (20):

$$F_{e1} = \frac{l_w}{2}\mathrm{Re}\int_0^{L_p} \bar{B}_1 e^{-\frac{x}{\alpha_1}} e^{-j\frac{\pi x}{\tau_e}} \left\{ \bar{J}_1 e^{-j\frac{\pi x}{\tau}} \right\}^* dx = \frac{mI^2 \mathrm{Re}\left\{\overline{K}_3 \bar{Z}_m\right\}}{v_s} \tag{25}$$

which becomes

$$P_{e1} = mI^2 \mathrm{Re}\left\{(1-s)\overline{K}_3 \bar{Z}_m\right\} \tag{26}$$

where

$$\overline{K}_3 = \frac{-1}{2P}\cdot\frac{1}{\tau\tau_e + j\alpha_1\pi\left(\tau - \tau_e\right)}\cdot\frac{\tau\left(\tau_e + j\alpha_1\pi\right)}{j\pi} \ . \tag{27}$$

The total input impedance of the entrance wave is $\overline{K}_1\overline{Z}_m$. For (26), the thrust (main) impedance is $\overline{K}_3\overline{Z}_m$. Therefore the impedance (which does not contribute to the thrust) can be defined as $(\overline{K}_1 - \overline{K}_3)\overline{Z}_m$; this is called the entrance-wave leakage impedance. These are illustrated in the series equivalent circuit in Fig. 5(a), where r_0 is primary resistance, and x_0 is primary leakage reactance. By the theory of electric machine [22], r_0 can be calculated by

$$r_0 = \rho_w L_{av} w_1 / s_w \tag{28}$$

where ρ_w is the primary winding resistivity, L_{av} the average length per turn winding, w_1 the number of per phase winding in series, and s_w the cross section area of per turn winding.

x_0 can be described by

$$x_0 = 0.158 f w_1^2 \frac{W_{pri}}{q}\frac{\lambda_s + \lambda_t + \lambda_e + \lambda_d}{P} \tag{29}$$

where f is primary source frequency, W_{pri} width of primary lamination, and λ_s, λ_t, λ_e, λ_d are the leakage magnetic conductances of primary slot, primary tooth termination, primary winding termination, and primary winding harmonics, respectively.

$\bar{Z}_m$ in absence of secondary leakage inductance and iron loss resistance can be composed of mutual reactance x_m and the secondary virtual resistance in parallel, as illustrated in Fig. 5(b).

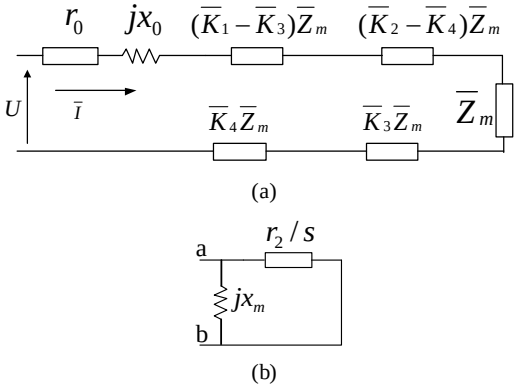

Fig. 5. Series equivalent circuit. (a) Per-phase circuit. (b) $\overline{Z}_m$ representation.

C. Exit-wave Impedance

The exit-wave electromagnetic power P_{m2} for the exit-end flux density wave can be obtained in a similar manner:

$$P_{m2} = mI^2\left(\overline{K}_2\overline{Z}_m\right) \tag{30}$$

where the constant is

$$\overline{K}_2 = -\frac{\alpha_2}{2P}\frac{\tau_e}{\tau\tau_e + j\alpha_2\pi(\tau+\tau_e)}. \tag{31}$$

The exit-wave thrust F_{e2} is

$$F_{e2} = \frac{mI^2\,\mathrm{Re}\left\{\overline{K}_4\overline{Z}_m\right\}}{v_s} \tag{32}$$

where

$$\overline{K}_4 = -j\frac{\alpha_1}{2P}\frac{\tau\left(\tau_e + j\alpha_2\pi\right)}{\alpha_2\pi\left[\tau\tau_e + j\alpha_2\pi\left(\tau+\tau_e\right)\right]}. \tag{33}$$

Again, we can divide the impedances into two parts. The exit-wave equivalent impedance is $\overline{K}_2\overline{Z}_m$, but the exit-wave main impedance is $\overline{K}_4\overline{Z}_m$, while the exit-wave leakage impedance is $(\overline{K}_2 - \overline{K}_4)\overline{Z}_m$. These are illustrated in Fig. 5(a).

D. Equivalent Circuit and Calculation

The total equivalent circuit is shown in Fig. 5. From (24), (27), (31) and (33) it can be shown (after considerable manipulation) that

$$(\overline{K}_1 + \overline{K}_2) = (\overline{K}_3 + \overline{K}_4) = \frac{-[(\alpha_1+\alpha_2)\tau_e^2 + j2\pi\alpha_1\alpha_2\tau\tau_e]}{2P[\tau\tau_e + j\alpha_1\pi\left(\tau-\tau_e\right)][\tau\tau_e + j\alpha_2\pi(\tau+\tau_e)]} \tag{34}$$

This illustrates that the sum of entrance and exit leakage impedances is zero because the total secondary input power ($(\overline{K}_1+\overline{K}_2)$ term) is equal to the total mechanical output power ($(\overline{K}_3+\overline{K}_4)$ term). Therefore the total equivalent longitudinal end-effect impedance Z_L is

$$\overline{Z}_L = \overline{K}_L\overline{Z}_m \tag{35}$$

where

$$\overline{K}_L = \overline{K}_1 + \overline{K}_2 \tag{36}$$

It is necessary to adjust the *z*-axis current in the secondary conducting sheet and *y*-axis flux density in the air-gap. These corrections are called the transversal different-width correction coefficient $\overline{K_t}$ and the air-gap fluxdensity correction coefficient $\overline{K_b}$. These are analogous to end-ring and fringing effects in rotating induction motors. The half-filled slots at the ends of the machine are accounted for by use of the half-filled slot correction coefficient K_p. These coefficients lead to small corrections in the fundamental and longitudinal end-effect impedances which make the performance analysis more accurate [27, 32]. Because the derivation procedures are interminable, we could summarize their brief expressions here.

The transversal different-width correction coefficient $\overline{K_t}$ is

$$\overline{K_t} = 1 + 0.767\frac{g}{a} + j\frac{sG\overline{T}}{a}\left(\frac{\tau}{\pi\overline{\gamma}} + g\right) \tag{37}$$

where a is half of primary width, $\overline{\gamma} = \sqrt{1+jsG}$, $\overline{T}$ is one function of machine structures and electric parameters described by

$$\overline{T} = \frac{1 - g\frac{\pi}{\tau}th(\frac{\pi}{\tau}c) + (g\frac{\pi}{\tau})^2(1-e^{-c/g})}{\left\{\begin{array}{l} cth(\frac{\pi}{\tau}a\overline{\gamma}) + \overline{\gamma}th(\frac{\pi}{\tau}c) + jsg\frac{\pi}{\tau}Gth(\frac{\pi}{\tau}c)\cdot cth(\frac{\pi}{\tau}\overline{\gamma}a) \\ -jsG(\frac{\pi}{\tau}g)^2 cth(\frac{\pi}{\tau}\overline{\gamma}a)(1-e^{-c/g}) \end{array}\right\}} \tag{38}$$

where c is half of difference between secondary- and primary-widths.

The air-gap flux density correction coefficient $\overline{K_b}$ is

$$\overline{K_b} = \frac{\pi g}{2\tau}\sqrt{1+jsG}\Big/th(\frac{\pi}{\tau}\frac{g}{2}\cdot\sqrt{1+jsG}) \tag{39}$$

The half-filled slot correction coefficient K_p is

$$K_p = \frac{(2P-1)^2}{4P^2 - 2P - Py_1m_1/q} \tag{40}$$

where y_1 the short pitch, q number of coil sides per phase per pole. For the influence of half-filled slots, K_p is smaller than 1.

Therefore, the modified fundamental impedance $\overline{Z}_{mc}$ is

$$\overline{Z}_{mc} = K_p\overline{K}_t\overline{K}_b\overline{Z}_m \tag{41}$$

and modified longitudinal end-effect impedance $\overline{Z}_{Lc}$ becomes

$$\overline{Z}_{Lc} = K_p\overline{K}_L\overline{Z}_m \tag{42}$$

This leads to the total impedance $\overline{Z}_t$ where

$$\overline{Z}_t = r_0 + jx_0 + \overline{Z}_{mc} + \overline{Z}_{Lc} \tag{43}$$

and the total thrust F is modified so that

$$F = \frac{mI^2\,\mathrm{Re}\left\{\overline{Z}_{mc} + \overline{Z}_{Lc}\right\}}{v_s} \tag{44}$$

The power factor cos φ is important in induction machines and this can be obtained from

$$\cos\varphi = \cos\left[\tan\left(\mathrm{Im}(\overline{Z})\Big/\mathrm{Re}(\overline{Z})\right)\right] \tag{45}$$

with the efficiency η calculated from

$$\eta = \mathrm{Re}\left\{\overline{Z}_{mc} + \overline{Z}_{Lc}\right\}\frac{(1-s)}{\mathrm{Re}\left\{\overline{Z}_t\right\}} \tag{46}$$

IV. Simulation and Experimentation

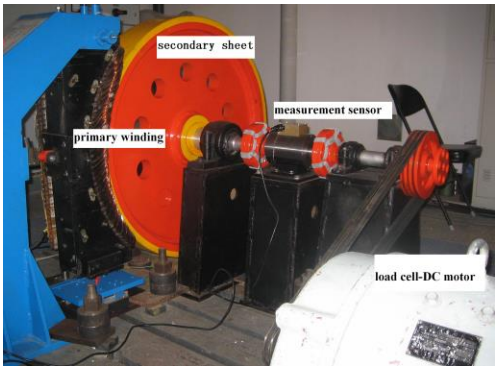

Fig. 6. SLIM prototype.

TABLE I
DIMENSIONS OF THE SLIM

Quantity	Value	Quantity	Value
Pole pitch	113 mm	Number of pole pairs	3
Secondary width	170 mm	Secondary sheet thickness	3 mm
Frequency	50 Hz	Primary length/width	450/100mm
Air gap length	7 mm	Primary phase voltage	220 V

In order to validate the series equivalent circuit analysis developed in the previous section, the algorithm was simulated and experimentally verified by the measurements on a SLIM prototype. The test rig is shown in Fig. 6. A rotating copper wheel arrangement was used to represent an infinitely long secondary sheet. The dimensions of the machine are given in Table I. The machine was a 4 kW 220 V 3-phase 50 Hz 6-pole linear induction machine with a synchronous speed of 13.3 m/s at 50 Hz. The supply was a variable-frequency inverter source so that a set of torque/speed curves could be obtained for a variety of frequencies.

The machine was loaded with a DC machine connected to the SLIM via belts. The DC machine could operate at any desired speed including operation at the synchronous speed (driven by the load in motoring mode). The system could measure the SLIM velocity, load power and thrust. Other variables such as the primary phase current and phase voltage were recorded using a power analyzer.

The simulation and experimental results for the thrust, power factor, and efficiency are given in Figs. 7 (a)-(d) for a constant input primary voltage of 220 V and a frequency of 50 Hz. The thrust/velocity curves shown in Fig. 7(a) are very similar to those of a rotating cage induction machine. The entry-wave thrust is negative except over a small slip region. The exit-wave thrust is very small over the whole operational region. The total calculated thrust curve, which is the sum of the three derived thrust components, agrees well with the measured points. The net thrust curve is lower than the fundamental curve due to the entry-wave thrust (apart from close to synchronism where the entry-thrust becomes positive). This illustrates that consideration of the fundamental flux wave only is insufficient for accurate analysis. In Figs. 7 (b) and (c), the power factor and efficiency are influenced slightly by the end effects in the lower speed region. As the velocity increases, the entry-wave thrust becomes positive near the synchronous speed, the end effects do begin to affect the power factor and efficiency to a greater extent. As the speed goes up, the air gap flux begins to distort affected by the end effect, and the secondary leakage inductance is bigger than that of low area. Hence, the experimental results of power factor deviate from the simulation results in certain degree for neglecting the secondary leakage inductance. These simulations are similar to the results found in [28]. A peak efficiency of about 60 % was found. While this seems low it is reasonable for a small robust induction machine.

Fig.7 (d) shows the thrust curves with a constant primary current of 15 A at varying frequencies from 0 to 40 Hz. The solid lines represent the thrusts without end effects in the simulation, the dashed lines represent the thrusts with end effects in the simulation and the markers represent the measured. The thrusts at low velocity (high slip) are not affected by the end effects. As the speed increases, the end effects have an increasing influence on the thrust across all the different constant-frequency curves.

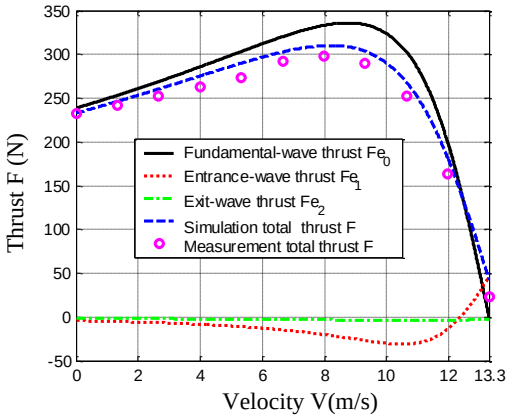

(a)

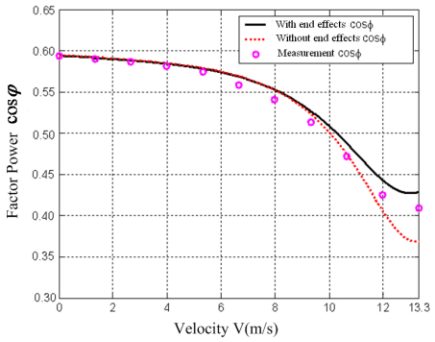

(b)

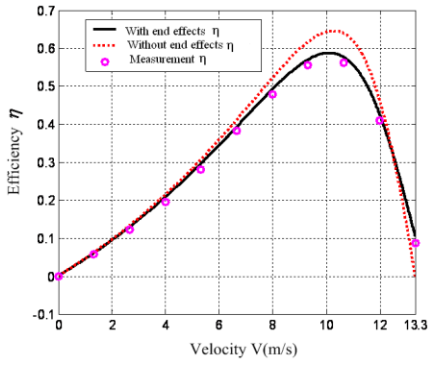

(c)

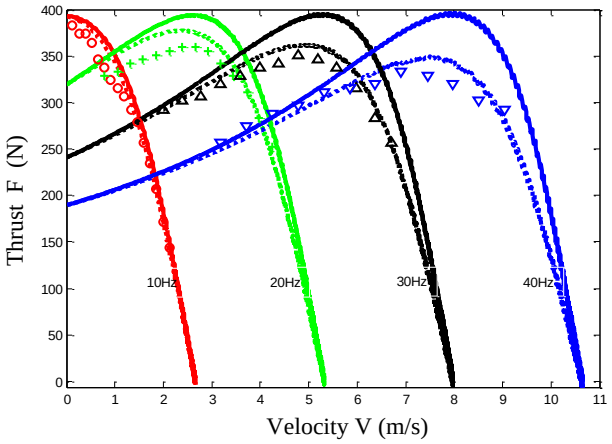

(d)

Fig.7 The simulation and experimental results. (a). Thrusts resulted from different air gap flux densities. (b). Power factor curves. (c). Efficiency curves. (d). Thrust curves in constant current and different frequencies.

V. Conclusion

This paper uses an equation for the air-gap flux density and develops an improved series equivalent circuit to calculate the performance, including thrust, efficiency and power factor, for a single-sides induction machine. The model is comprehensive and considers the longitudinal end-effects, transversal edge-effects and half-filled slots. Test data from a 4 kW SLIM prototype is put forward to validate the simulation results and good correlation was found. This model could also be implemented to simulate high power SLIMs and would be useful for designing linear machines for applications such a rapid transport or even low-speed low-head hydro water wheels where it would be used in generating mode.

Appendix I

Derivation of Flux Density and Electrical Field Intensity Coefficients

Based on the air gap flux density equation from the one dimensional model as illustrated in Section II, the solution of b_y can be expressed by

$$b_y = b_y(x,t) = \mathrm{Re}\left\{\left(\bar{B}_0 e^{-j\frac{\pi x}{\tau}} + \bar{B}_1 e^{-\frac{x}{\alpha_1}} e^{-j\frac{\pi x}{\tau_e}} + \bar{B}_2 e^{\frac{x}{\alpha_2}} e^{j\frac{\pi x}{\tau_e}}\right) e^{j\omega t}\right\} \tag{A-1}$$

The first part is the flux density normal wave, similar to that of rotary machine, whose coefficient is

$$\bar{B}_0 = \frac{j\tau\mu_0 \bar{J}_1}{g\pi(1+jsG)} \tag{A-2}$$

The coefficient is the same as B_s in Ref. [26]. The secondary part is the entry end effect wave, and the third part is the exit end effect wave. They involve two unknown coefficients, $\bar{B}_1$ and $\bar{B}_2$, which are to be determined from two boundary conditions as shown below.

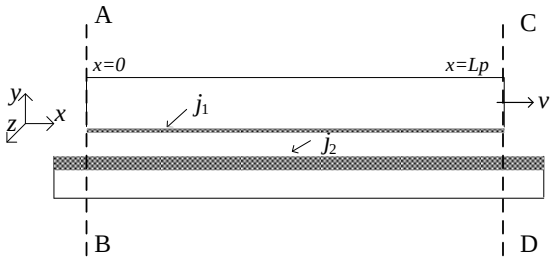

Fig. A-1 Magnetic barrier without considering the leakage flux density in the primary end.

Actually, the flux densities in both primary ends attenuate fast to zero. Take the right end for example. In theory, we can find the surface outside the end that the flux density is zero, but the calculation is greatly complicated. In most cases, it is reasonable to neglect the leakage flux density in the end, which could bring some certain error but agree with engineering requirement. Hence, we suppose the surface that the end flux density is zero is coincident with the primary end, and the surface here is called as magnetic barrier surface. In Fig. A-1, there are two magnetic barrier surfaces, AB, CD, located at the primary ends respectively, which have the following fundamental traits.

(1) The normal component of the flux density in the magnetic barrier inner surface is zero, but the tangential component can be arbitrary.

(2) All the SLIM field quantities are distributed in the space between AB and CD.

(3) The surface integral of the air gap flux density between AB and CD is zero.

According to the above third trait, there is no leakage flux at both primary ends, and through the air gap, the flux only leaves and enters the back iron. Hence, we can have **the first boundary condition** as

$$\int_0^{L_p} b_y(x,t)dx = 0 \tag{A-3}$$

In the one dimensional model, the primary excited current density has only z component, then by the field theory, the magnetic vector potential, $\vec{A}$, also has only z component described by,

$$\vec{A} = \vec{K}a_z(x,y,z,t) \tag{A-4}$$

Based on the Coulomb gauge, we know that,

$$\vec{B} = \nabla \times \vec{A} \tag{A-5}$$

$$\nabla \bullet \vec{B} = 0 \tag{A-6}$$

Because the flux density outside the magnetic barrier surface is zero, we can know that the z component of magnetic vector potential in this space is

$$a_z = a_z(t) \tag{A-7}$$

Equation (A-7) indicates that a_z is constant in one definite time, not change with respect with the position. For the case that the magnetic field energy is not infinite, we can know the a_z in the magnetic barrier outside space is zero expressed by,

$$a_z = 0 \tag{A-8}$$

The space electric field intensity without the effect of electrostatic field can be described by,

$$\vec{E} = -\frac{\partial \vec{A}}{\partial t} \quad \text{(A-9)}$$

So it is easy to draw another conclusion about magnetic barrier surface by combining (A-8) and (A-9):

(4) The electric field intensity, $\vec{E}$, outside the magnetic barrier surface is zero.

According to the boundary condition, the tangential component of electric field intensity in the magnetic barrier surface is zero. We can draw a surface in parallel with *xy*, and make it intersect with the secondary sheet. The secondary current density surface integral in the cross section is zero, i.e.

$$\int_0^{L_p} j_2(x,t)dx = 0 \quad \text{(A-10)}$$

Hence, we can get the fifth trait of the magnetic barrier surface described as,

(5) The surface integral of electric field intensity between the two magnetic barrier surfaces, AB and CD, is zero. This is **the second boundary condition**.

Moreover, we can derive the mathematical expressions for the second boundary condition so as to gain the numerical equations for $\overline{B}_1$, $\overline{B}_2$, $\overline{E}_0$, $\overline{E}_1$, and $\overline{E}_2$.

The three fundamental electromagnetic field equations in SLIM are summarized as,

$$\nabla \times \vec{E} = -\frac{\partial \vec{B}}{\partial t} \quad \text{(A-11)}$$

$$\nabla \cdot \vec{B} = 0 \quad \text{(A-12)}$$

$$\nabla \cdot \vec{H} = \vec{J} \quad \text{(A-13)}$$

In one dimensional model, (A-12) can be simplified as,

$$\frac{\partial e_z}{\partial x} = \frac{\partial b_y}{\partial t} \quad \text{(A-14)}$$

Here the coordination is placed on the primary, which is comparatively static with the moving part. Therefore, the speed term, $v\frac{\partial b_y}{\partial x}$, is not included in (A-14).

Then the *z* component of electric field intensity can be expressed by

$$e_z = \int \frac{\partial b_y}{\partial t}dx + C(t) \quad \text{(A-15)}$$

As the tangential component of electrical field intensity in the inner magnetic barrier surface is zero, we can acquire

$$\begin{cases} \int \frac{\partial b_y}{\partial t}dx\,|_{x=0} + C(t) = 0 \\ \int \frac{\partial b_y}{\partial t}dx\,|_{x=L_p} + C(t) = 0 \end{cases} \quad \text{(A-16)}$$

Then e_z between AB and CD can be described as

$$e_z = \int_0^x \frac{\partial b_y}{\partial t}dx \quad \text{(A-17)}$$

Based on the fifth trait of magnetic barrier surface, we can have

$$\int_0^{L_p} e_z dx = 0 \quad \text{(A-18)}$$

Moreover, substituting (A-17) into (A-18), the mathematical equation for the second boundary condition can be rewritten as,

$$\int_0^{L_p}\int_0^{x'} \frac{\partial b_y}{\partial t}dxdx' = 0 \quad \text{(A-19)}$$

Substituting (A-1) into (A-3) and (A-19) respectively, we can get

$$\begin{cases} \frac{e^{\xi_1 L}-1}{\xi_1}\overline{B}_1 + \frac{e^{\xi_2 L}-1}{\xi_2}\overline{B}_2 = 0 \\ (\frac{e^{\xi_1 L}-1}{\xi_1^2} - \frac{L}{\xi_1})\overline{B}_1 + (\frac{e^{\xi_2 L}-1}{\xi_2^2} - \frac{L}{\xi_2})\overline{B}_2 = \frac{L}{\xi_0}\overline{B}_0 \end{cases} \quad \text{(A-20)}$$

where $\xi_0 = -j\frac{\pi}{\tau}$, $\xi_1 = -\frac{1}{\alpha_1} - j\frac{\pi}{\tau_e}$, $\xi_2 = \frac{1}{\alpha_2} + j\frac{\pi}{\tau_e}$.

Then we can get the expressions for $\overline{B}_1$ and $\overline{B}_2$ by

$$\begin{cases} \overline{B}_1 = \frac{\Delta_x}{\Delta}\overline{B}_0 \\ \overline{B}_2 = \frac{\Delta_y}{\Delta}\overline{B}_0 \end{cases} \quad \text{(A-21)}$$

where $\Delta = \begin{vmatrix} \frac{e^{\xi_1 L_p}-1}{\xi_1} & \frac{e^{\xi_2 L_p}-1}{\xi_2} \\ \frac{e^{\xi_1 L_p}-1}{\xi_1^2} - \frac{L_p}{\xi_1} & \frac{e^{\xi_2 L_p}-1}{\xi_2^2} - \frac{L_p}{\xi_2} \end{vmatrix}$, $\Delta_x = -\frac{e^{\xi_2 L_p}-1}{\xi_2}\frac{L_p}{\xi_0}$, $\Delta_y = -\frac{e^{\xi_1 L_p}-1}{\xi_1}\frac{L_p}{\xi_0}$, By further simplification, (A-21) can be described as

$$\begin{cases} \overline{B}_1 = -\frac{\frac{1}{\alpha_1} + j\frac{\pi}{\tau_e}}{j\frac{\pi}{\tau}}\overline{B}_0 \\ \overline{B}_2 = \frac{\frac{1}{\alpha_2} + j\frac{\pi}{\tau_e}}{j\frac{\pi}{\tau}e^{(\frac{1}{\alpha_2}+j\frac{\pi}{\tau_e})L_p}}\overline{B}_0 \end{cases} \quad \text{(A-22)}$$

Furthermore, by combining (A-1) and (A-17), we can get the expressions for the electric field intensity coefficients, i.e. $\overline{E}_0$, $\overline{E}_1$, and $\overline{E}_2$, in the following.

$$\begin{cases} \overline{E}_0 = -v_s\overline{B}_0 \\ \overline{E}_1 = -\frac{j\omega\overline{B}_1\alpha_1\tau_e}{(\tau_e + j\pi\alpha_1)} \\ \overline{E}_2 = \frac{j\omega\overline{B}_2\alpha_2\tau_e}{\tau_e + j\pi\alpha_2} \end{cases} \quad \text{(A-23)}$$

Hence, e_z, which is similar to that of flux density, also includes three parts, which are functions of time and x position that are described as

$$e_z(x,t)=\mathrm{Re}\left\{\overline{E}_0 e^{j\left(\omega t-\frac{\pi x}{\tau}\right)}+\overline{E}_1 e^{-\frac{x}{\alpha_1}} e^{j\left(\omega t-\frac{\pi x}{\tau_e}\right)}+\overline{E}_2 e^{\frac{x}{\alpha_2}} e^{j\left(\omega t+\frac{\pi x}{\tau_e}\right)}\right\} \quad \text{(A-24)}$$

APPENDIX II
DERIVATION OF GOODNESS FACTOR

In one SLIM, the goodness factor, G, should express the ability of a machine to convert power from one form to another. Generally, power on the mechanical side is the product of force and velocity, and force on the electrical side is the product of current and magnetic flux. The electric circuit enables an electromotive force (EMF) to produce a current, and the magnetic circuit enables a current to produce a flux. Hence, G can be defined as

$$G \propto (I/E)(\phi/I') \quad \text{(A-25)}$$

where I/E, named as a unitary current by EMF, is equal to $1/R$ from Ohm's law, and ϕ/I', named as a unitary flux by current, is the inductance L. The product of $(I/E)(\phi/I')$, similar to $I\phi$, can be considered as the work done by force.

Actually, G should express the ability of the machine to convert the power which is the product of velocity (dependent on primary angular frequency ω) and force. Therefore, G that must contain ω can be simplified by

$$G=\omega\frac{L}{r} \quad \text{(A-26)}$$

In one dimensional model, the SLIM performance in absence of secondary leakage inductance is dependent on the mutual inductance, L_m, and secondary equivalent resistance, r_2. Therefore, (A-26) can be rewritten by

$$G=\omega\frac{L_m}{r_2}=\omega T_r \quad \text{(A-27)}$$

where T_r is the time constant of secondary circuit. It is necessary to translate the expression of G into terms of the physical dimensions of a machine so as to assess the performance in the design procedure. It is assumed that the fundamental airgap flux density and secondary equivalent current sheet can be expressed by,

$$b_0=B_0\cos(\frac{\pi}{\tau}x) \quad \text{(A-28)}$$

$$j_2=J_2\sin(\frac{\pi}{\tau}x) \quad \text{(A-29)}$$

where B_0 and J_2 are the amplitudes of primary fundamental flux density and secondary equivalent current. From the electrical machine theory, the amplitude of air gap fundamental magnetomotive force, *MMF*, can be described as

$$MMF=\frac{g}{\mu_0}B_0=\int_0^{\frac{\tau}{2}} j_2 dx \quad \text{(A-30)}$$

Hence, we can derive the relationship between B_0 and J_2 by (A-29) and (A-30)

$$B_0=\frac{\mu_0\tau}{\pi\delta}J_2 \quad \text{(A-31)}$$

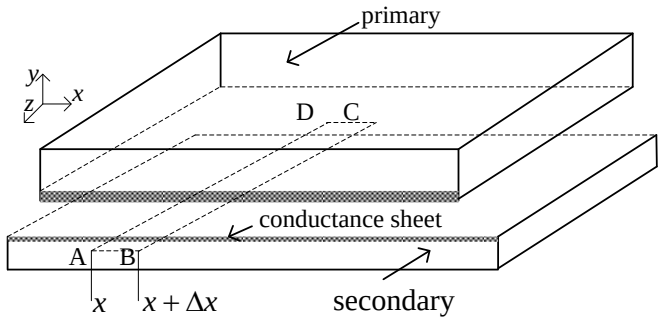

Fig.A-2 Derivation of goodness factor.

The fluxsurrounded by the close loop in Fig.A-2, ABCD, can be expressed by

$$\Delta\phi=W_{\mathrm{sec}}\int_x^{x+\Delta x} b_0 dx=W_{\mathrm{sec}}B_0\Delta x\cos(\frac{\pi}{\tau}x) \quad \text{(A-32)}$$

where W_{sec} is the secondary width.

Moreover, it is supposed that the resistance of ABCD is Δr, then the voltage drop of ABCD with current j_2 can be deduced by

$$\begin{aligned}\Delta r j_2 &= W_{\mathrm{sec}}\rho[J_2\sin(\frac{\pi}{\tau}x)-J_2\sin(\frac{\pi}{\tau}x+\Delta x)] \\ &= W_{\mathrm{sec}}\rho J_2\frac{\pi}{\tau}\Delta x\sin(\frac{\pi}{\tau}x)\end{aligned} \quad \text{(A-33)}$$

Supposing that the inductance of ABCD is ΔL, then T_r in (A-27) can be deduced by

$$T_r=\frac{\Delta L}{\Delta r}=\frac{\Delta L}{\Delta r}\frac{j_2}{j_2}=\frac{\Delta\phi}{\Delta r j_2} \quad \text{(A-34)}$$

After substituting (A-31), (A-32), (A-33) into (A-34), T_r can be rewritten as

$$T_r=\frac{\mu_0\tau^2}{\pi^2\rho g} \quad \text{(A-35)}$$

By combining (A-27) and (A-35), the goodness factor G can be described as

$$G=\frac{\sigma\mu_0\omega\tau^2}{g\pi^2} \quad \text{(A-36)}$$

ACKNOWLEDGMENT

Many thanks go to Prof. Xialing Long, Prof. Yumei Du, Dr. Jinqi Ren, and Engineer Wu Wang in Institute of Electrical Engineering, Chinese Academy of Sciences, China, and David G. Dorrell in University of Technology Sydney, Australia for their great assistance for our work in this paper.

REFERENCES

[1]. J. Duncan, "Linear induction motor equivalent circuit model," *IEE Proc.*, vol. 130, part B, no.1, pp.51-57, Jan.1983.

[2]. Tsuyoshi Higuchi and Sakutaro Nonaka, "On the design of high efficiency linear induction motors for linear metro," *Electrical Engineering in Japan*, vol. 137, no. 2, pp. 36-43, Aug. 2001.
[3]. C. Jung Soo and B. Yoon Su, "Magnetically-levitated steel-plate conveyance system using electromagnets and a linear induction motor," *IEEE Trans. Magn.*, vol. 44, pp. 4171-4174, Nov. 2008.
[4]. E. R. Laithwaite, "Linear electric machines - a personal view," *Proceedings of the IEEE*, vol. 63, pp. 250-290, Feb. 1975.
[5]. T. R. F. Neto and R. S. T. Pontes, "Design of a counterweight elevator prototype using a linear motor drive," in *IEEE Int. conf. Electric Machines & Drives*, 2007, pp. 376-380.
[6]. N. Shamsuddeen, Ankit Ashok, Rajendrakumar J, *et al.*, "Design and analysis of annular linear induction pump (ALIP)," in *IEEE Proc. Int. Conf. Power System Technology*, 2008, pp. 1-5.
[7]. P. R. Austin and A. R. Eastham, "Helically wound linear induction pump for molten nonferrous metals," *IEEE Trans. Ind. Appl.*, vol. IA-21, pp. 738-748, May/Jun.1985.
[8]. D. C. Meeker and M. J. Newman, "Indirect vector control of a redundant linear induction motor for aircraft launch," *Proceedings of the IEEE*, vol. 97, pp. 1768-1776, Nov. 2009.
[9]. R. Haghmaram and A. Shoulaie, "Transient modeling of multiparallel tubular linear induction motors," *IEEE Trans. Magn.*, vol. 42, pp. 1687-1693, Jun. 2006.
[10]. P. Joon-Hyuk and B. Yoon Su, "Design and analysis of a maglev planar transportation vehicle," *IEEE Trans. Magn.*, vol. 44, pp. 1830-1836, Jul. 2008.
[11]. L. Byung-Jun, Dae-Hyun Koo, and Yun-Hyun Cho, "Investigation of linear induction motor according to secondary conductor structure," *IEEE Trans. Magn.*, vol. 45, pp. 2839-2842, Jun. 2009.
[12]. R. Hellinger and P. Mnich, "Linear motor-powered transportation: history, present status, and future outlook," *Proceedings of the IEEE*, vol. 97, pp. 1892-1900, Nov. 2009.
[13]. R. Thornton, *et al.*, "Linear motor powered transportation," *Proceedings of the IEEE*, vol. 97, pp. 1754-1757, Nov. 2009.
[14]. J. Gustafsson, "Vectus-intelligent transport," *Proceedings of the IEEE*, vol. 97, pp. 1856-1863, Nov. 2009.
[15]. I. E. Davidson and J. F. Gieras, "Performance analysis of a shaded-pole linear induction motor using symmetrical components, field analysis, and finite element method," *IEEE Trans. Energy Convers.* , vol.15, no.1, pp. 24-29, Mar. 2000.
[16]. S. Nonaka and T. Higuchi, "Design of single-sided linear induction motors for urban transit," *IEEE Trans. Veh. Techno.*, vol.37, no.3, pp. 167-173, Aug. 1988.
[17]. A. K. Rathore and S. N. Mahendra, "Simulation of secondary flux oriented control of linear induction motor considering attraction force and transverse edge effect," in *Pro. Inter. Conf. on Electrical Engineering Proceeding*, pp.158-163, 2003.
[18]. J. F. Gieras, G. E. Dawson and A. R. Eastham, "A new longitudinal end effect factor for linear induction motors," *IEEE Trans. Magn.*, EC-2(1), pp.152-159, Mar.1987.
[19]. Sung Chan Ahn, Jung Ho Lee, Dong Seok Hyun, "Dynamic characteristic analysis of LIM using coupled FEM and control algorithm," *IEEE Trans. Magn.*, vol.36, no.4, pp. 1876-1880 , Jul. 2000.
[20]. J. F. Gieras, *Linear Lnduction Drives*, Oxford: Clarendon, 1994.
[21]. S.A. Nasar and I.Boldea, *Electric Drives*, CRC Press, 1999.
[22]. I. Boldea and S. A. Nasar, *Linear Motion Electromagnetic Systems*, New York: Wiley, 1985.
[23]. J.-H. Sung and K. Nam, "A new approach to vector control for a linear induction motor considering end effects," in *Proc. IEEE Industry Applications Conf.* vol.4, pp.2284-2289, 1999.
[24]. K. Venkataratnam and A. B. Chattopadhyay, "Analysis of electromagnetic forces in a levitated short rotor LIM-Part II: lateral stabilization," *IEEE Trans. Energy Convers.*, vol.17, no.1, pp. 102-106, Mar. 2002.
[25]. S. Yamamura, *Theory of Linear Induction Motors*, Tokyo Press, 1978.
[26]. S. Yamamura, H. Ito and Y. Ishulawa, "Theories of the linear induction motor and compensated linear induction motor," *IEEE Trans. Power App. and Syst.*, vol. PAS-91, no. 4, pp 1700-1710, Dec.1971.
[27]. X. Long, *Theory and Magnetic Design Method of Linear Induction Motor* (in Chinese), China: Science Publishing Company, 2006.
[28]. Jeong-Hyoun Sung, and Kwanghee Nam, "A new approach to vector control for a linear induction motor considering end effects," in *Proc. IEEE IAS Annual Meeting*, 1999, pp. 2284-2289.
[29]. G. Kang and K. Nam, "Field-oriented control scheme for linear induction motor with the end effect," *IEE Proceeding on Electrical Power Application*, vol. 152, no. 6, pp. 1565-1572, Nov. 2005.
[30]. W. Xu, J.G. Zhu, Y.G. Guo, Y.C. Zhang, and Y. Wang, "Equivalent circuits for single-sided linear induction motors," in *Proc. IEEE Energy Conversion Congress and Exposition*, Sept. 2009, pp.1288-1295.
[31]. Y.Mori, S. Torii, and D. Ebihara, "End effect analysis of linear induction motor based on the wavelet transform technique," *IEEE. Trans. Magn.*, vol. 35, no. 5, pp. 3739-3741, Sept. 1999.
[32]. W. Xu, J.G. Zhu, Y.C. Zhang, D.G. Dorrell, and Y.J. Li, "An improved series equivalent circuit of a single-sided linear induction motor," in *Proc. IEEE Industrial Electronics Society*, Nov. 2009, pp.1-6.

Wei Xu (M'09) was born in Chongqing, China in 1980. He received the B.E. & B.A., and M.E. degrees from Tianjin University, China, in 2002 and 2005, and the Ph.D. degree from the Institute of Electrical Engineering, Chinese Academy of Sciences, in 2008, respectively, all in electrical engineering.

He is currently one postdoctoral fellow with the Center for Electrical Machines and Power Electronics, University of Technology Sydney, where his research is supported by Early Career Researcher Grant and partly supported by Chancellor's Postdoctoral Research Fellowship, both at UTS. He is greatly excited by electromagnetic design and performance analysis of linear/rotary machines, including induction, permanent magnet, switched reluctance, and other emerging novel structure machines.

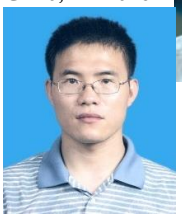

Jian Guo Zhu (S'93-M'96-SM'03) received his B.E. in 1982 from Jiangsu Institute of Technology, China, M.E. in 1987 from Shanghai University of Technology, China, and Ph.D in 1995 from University of Technology, Sydney (UTS), Australia.

He currently holds the positions of Professor of Electrical Engineering and Head for School of Electrical, Mechanical and Mechatronic Systems at UTS, Australia. His research interests include electromagnetics, magnetic properties of materials, electrical machines and drives, power electronics, and renewable energy systems.

Yongchang Zhang received the B.S. degrees from Chongqing University, China, in 2002 and the Ph.D. degree from Tsinghua University, in 2009, respectively, both in electrical engineering.

He is currently a postdoctoral fellow with the University of Technology, Sydney. His research interests include sensorless and high performance control of AC motor drives, control of multilevel converters, pulsewidth modulation, PWM rectifier, advanced digital control with realtime implementation.

Yaohua Li was born in Henan, China, in 1966. He received the Ph.D. degree from Tsinghua University, Beijing, China, in 1994.

From 1995 to 1997, he was a Postdoctoral Research Fellow with the Institute of Electrical Machine, Technical University of Berlin, Berlin, Germany. In 1997, he joined the Institute of Electrical Engineering, Chinese Academy of Sciences, Beijing, where he is currently a Professor and the Director of the Laboratory of Power Electronics and Electrical Drives. His research fields include the analysis and control of electrical machines, power electronics, etc.

Yi Wang received the B.Eng. and M.Sc. degrees in electrical engineering from Huazhong University of Science and Technology, Wuhan, China, in 2004 and 2007, respectively. He is currently working toward the Ph.D. degree in School of Electrical, Mechanical and Mechatronic Systems, University of Technology, Sydney, Australia.

His research interests include power electronics, modeling and control of electrical drives, in particular, permanent-magnet synchronous machines.

Youguang Guo (S'02-M'05-SM'06) was born in Hubei, China in 1965. He received the B.E. degree from Huazhong University of Science and Technology (HUST), China in 1985, the M.E. degree from Zhejiang University, China in 1988, and the Ph.D degree from University of Technology, Sydney (UTS), Australia in 2004, all in electrical engineering.

From 1988 to 1998, he lectured in the Department of Electric Power Engineering, HUST. From March 1998 to July 2008, he worked as visiting research fellow, PhD candidate, postdoctoral fellow and research fellow in the Center for Electrical Machines and Power Electronics, Faculty of Engineering, UTS. He is currently a lecturer at the School of Electrical, Mechanical and Mechatronic Systems, UTS.

His research fields include measurement and modeling of magnetic properties of magnetic materials, numerical analysis of electromagnetic field, electrical machine design and optimization, power electronic drives and control. In these fields, he has published over 230 refereed technical papers including 110 journal articles.